

Optimized controlled-Z gates for two superconducting qubits coupled through a resonator

This content has been downloaded from IOPscience. Please scroll down to see the full text.

2014 Supercond. Sci. Technol. 27 014001

(<http://iopscience.iop.org/0953-2048/27/1/014001>)

View [the table of contents for this issue](#), or go to the [journal homepage](#) for more

Download details:

IP Address: 129.81.226.78

This content was downloaded on 30/08/2014 at 03:04

Please note that [terms and conditions apply](#).

Optimized controlled-Z gates for two superconducting qubits coupled through a resonator

D J Egger¹ and F K Wilhelm^{1,2}

¹ Theoretical Physics, Saarland University, D-66123 Saarbrücken, Germany

² IQC and Department of Physics and Astronomy, University of Waterloo, ON, N2L 3G1, Canada

E-mail: egger.d.j@gmail.com

Received 28 June 2013, in final form 22 October 2013

Published 26 November 2013

Abstract

Superconducting qubits are promising candidates for building a quantum computer. A continued challenge for fast yet accurate gates is to minimize the effects of decoherence. Here we apply numerical methods to design fast entangling gates, specifically the controlled-Z, in an architecture where two qubits are coupled via a resonator. We find that the gates can be sped up by a factor of two and reach any target fidelity. We also discuss how systematic errors arising from experimental conditions affect the pulses and how to remedy them, providing a strategy for the experimental implementation of our results. We discuss the shape of the pulses, their spectrum and symmetry.

(Some figures may appear in colour only in the online journal)

1. Introduction

Superconducting quantum devices provide a promising route to creating a quantum computer [1]. In many applications, the quantum states are implemented with qubits [2] connected by strip-line resonators [3]. The qubit is engineered to have a strong dipole interaction with the cavity. This strong coupling allows many Rabi oscillations between qubits and resonators before the quantum states decohere. Although coherence times have significantly improved over the past decade [4–10] the quantum operations should be implemented quickly to mitigate the effects of decoherence. Additionally, if a full scale quantum computer were to be built, many quantum operations have to be performed and thus gate speed is crucial to limit computation times [11]. Human-engineered artificial atoms have great flexibility and controllability [12, 1, 13–15]. Therefore there is much to be gained by using optimal control theory methods [16–18] to engineer the control pulses producing the gates.

In this work we apply optimal control to find a fast and accurate pulse shape to speed up a controlled-Z gate between two qubits connected by a resonator [19–28]. The controlled-Z completes a universal gate set together with single-qubit rotations [29]. The setting is motivated by superconducting qubits but has analogies in atomic physics [30], quantum dot [31, 32], and other resonator-based

systems. We demonstrate the feasibility of these pulses by taking into account bandwidth limitations imposed by the experiment and provide a methodology for removing systematic errors that can practically affect the application of the control pulse.

The plan of the paper is as follows: in section 2 we describe the system setting as well as conventional analytic methods [33] to create CZ gates. Here we show that those constructions are strongly limited by low qubit anharmonicity. Section 3 describes the implementation of optimal control to this system and its results and section 4 discusses potential error sources and their mitigation.

2. System

2.1. Hamiltonian

In the following $\hbar = 1$. The system of interest is made of two qubits coupled to a bus resonator, where the qubits are sufficiently far apart so that their direct coupling can be neglected. They are modelled by three-level nonlinear oscillators. The third level accounts for leakage and in the case of the CZ gate can be populated to perform the gate. The individual qubit Hamiltonians are

$$\hat{H}_{qk} = \Delta_k |2\rangle_k \langle 2| + \omega_k \hat{\sigma}_k^+ \hat{\sigma}_k^-, \quad (1)$$

where $\hat{\sigma}_k^+$ and $\hat{\sigma}_k^-$ respectively create and destroy one excitation in qubit k , $\hat{\sigma}_k^\pm = \sum_n |n \pm 1\rangle_{kk} \langle n|$. ω_k is the $0 \leftrightarrow 1$ transition frequency and Δ_k is the anharmonicity. The bus, with transition frequency ω_b , is harmonic and possess three levels: $\hat{H}_b = \omega_b \hat{a}_b^\dagger \hat{a}_b$. The dipolar coupling strength between the bus and qubit k satisfies $g_k \ll \omega_k$ and therefore the rotating wave approximation holds. The system's total Hamiltonian in this approximation is

$$\hat{H} = \omega_b \hat{a}_b^\dagger \hat{a}_b + \sum_{k=1}^2 \left[\Delta_k |2\rangle_{kk} \langle 2| + \omega_k \hat{\sigma}_k^+ \hat{\sigma}_k^- + \frac{g_k}{2} (\hat{\sigma}_k^+ \hat{a}_b + \hat{\sigma}_k^- \hat{a}_b^\dagger) \right].$$

By the transformation $\hat{H}^R = R^\dagger \hat{H} R - i \dot{R}^\dagger R$ where

$$\hat{R} = \left(\sum_{j=0}^2 \exp\{-ij\omega_b t\} |j\rangle \langle j| \right)^{\otimes 3}, \quad (2)$$

we move to the rotating frame in which energies are measured with respect to the transition frequency of the bus. The Hamiltonian is

$$\hat{H}^R = \sum_{k=1}^2 \left[\delta_k(t) \hat{n}_k + \Delta_k |2\rangle_{kk} \langle 2| + \frac{g_k}{2} (\hat{\sigma}_k^+ \hat{a}_b + \hat{\sigma}_k^- \hat{a}_b^\dagger) \right] \quad (3)$$

where $\hat{n}_k = \hat{\sigma}_k^+ \hat{\sigma}_k^-$ is the number operator for qubit k . The time dependence of the qubit–resonator detuning $\delta_k(t) = \omega_k(t) - \omega_b$ is made explicit to indicate the controls. The energy levels are sketched in figure 1. The Hilbert space size is 27-dimensional and Hamiltonian (3) conserves the number of excitations. We make use of this to reduce the size of the Hilbert space, since only computational states—states in which the qubits have at most one excitation—are of interest as well as the states that can be reached from these computational states. Therefore we only need to study the ten states with at most two quanta. The model is valid for transmons [34] and phase qubits [35]. When dealing with the latter, the anharmonicity is a function of the qubit transition frequency and therefore a function of the controls $\Delta_k = \Delta_k(\delta_k(t))$. However, for transmon qubits, in the limit of large Josephson energy to charge energy it can be kept constant [34] to sufficient precision.

2.2. Analytic CZ gate

In the qubit–bus–qubit system, the entangling gate needed to form a universal set of gates is the CZ defined by $|ij\rangle \mapsto (-1)^{ij} |ij\rangle$. It is realized with two iSWAPs and a conditional rotation through a $|2\rangle$ state [33]. A sketch of the pulse sequence is shown in figure 2. The 2π rotation through the $|2\rangle$ state only takes place when both qubits are in the $|1\rangle$ state and leaves a phase of π onto that state; this can entangle the qubits. This 2π rotation is referred to as the Strauch gate [36]. This sequence is slow due to the shifting of states in and out of the resonator. An improved analytic pulse sequence based on few parameters has been found in Ghosh *et al* [28]. This work considers an alternate approach based on numerical methods.

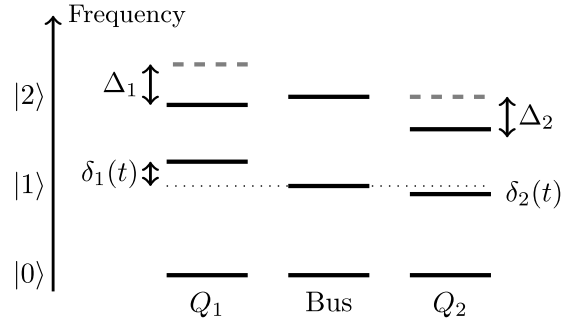


Figure 1. Sketch of the system where each element has three levels. The bus is harmonic and the qubits have anharmonicity Δ_k , which can be dependent on the detunings in the case of the phase qubits.

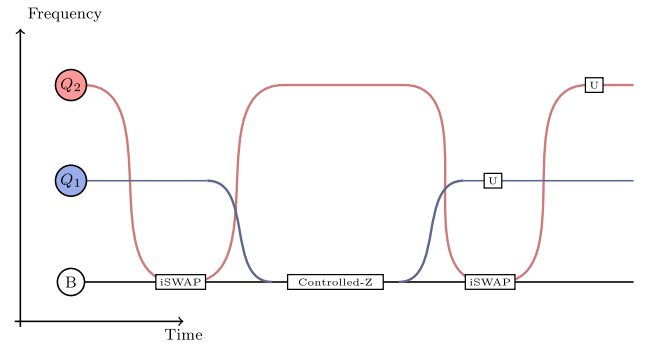


Figure 2. Sketch showing how the qubit's frequency is changed as a function of time to create a CZ gate.

2.3. Three-level qubit and bus: limitations from weak anharmonicity

The fidelity of a Strauch gate is degraded by the presence of other levels in the system. To illustrate this we consider a simplified model compared to Hamiltonian (3); a three-level anharmonic qubit coupled to a resonator

$$\hat{H}_{QB} = \underbrace{\omega_b (\hat{a}^\dagger \hat{a} + \hat{\sigma}^+ \hat{\sigma}^-)}_{\hat{H}_I} + \underbrace{\delta \hat{\sigma}^+ \hat{\sigma}^- + \Delta |2\rangle \langle 2| + \frac{g}{2} (\hat{\sigma}^+ \hat{a} + \hat{\sigma}^- \hat{a}^\dagger)}_{\hat{H}_{II}} \quad (4)$$

where $\delta = \omega_q - \omega_b$. This Hamiltonian conserves excitation number and thus is block diagonal with at most 3×3 blocks. For the block with n excitations \hat{H}_I is diagonal with identical values of $n\omega_b$. Focusing on $n = 2$ the bare states are $|2, 0\rangle$, $|1, 1\rangle$ and $|0, 2\rangle$. The Hamiltonian is

$$\hat{H}^{(2)} = \begin{bmatrix} 2\omega_b + 2\delta + \Delta & \sqrt{2}g & 0 \\ \sqrt{2}g & 2\omega_b + \delta & \sqrt{2}g \\ 0 & \sqrt{2}g & 2\omega_b \end{bmatrix}. \quad (5)$$

An example of the eigenvalues of $\hat{H}^{(2)}$, for two different anharmonicities, are shown in figure 3. The fine black lines represent energies of the uncoupled system, i.e. the bare states. A controlled-Z gate is made by a 2π rotation through the

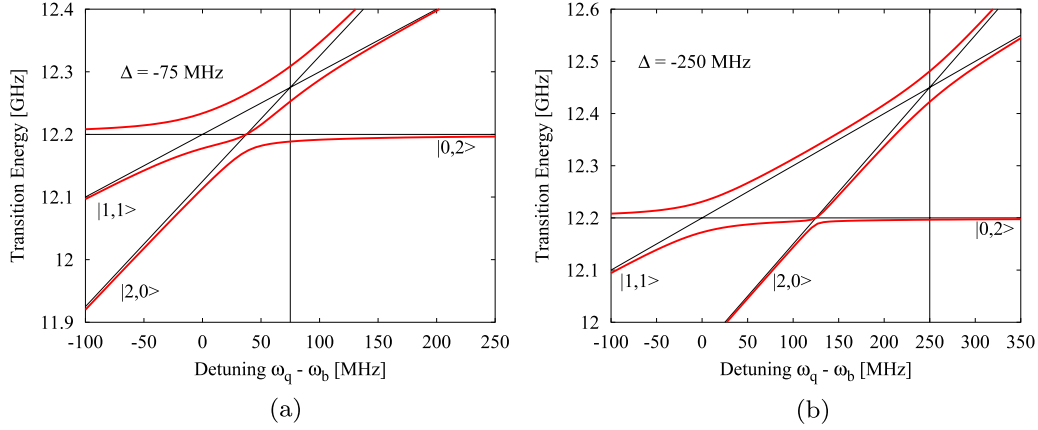


Figure 3. Energy of the dressed states in the three-level Jaynes–Cummings model with $\omega_b = 6.1$ GHz and $T_{\text{swap}} = 12$ ns, i.e. the time it takes to swap a single excitation between the qubit and the bus. The three light black lines indicate the bare states whilst the vertical black line is $-\Delta/2$. (a) Dressed states with -75 MHz anharmonicity and (b) dressed states with -250 MHz anharmonicity.

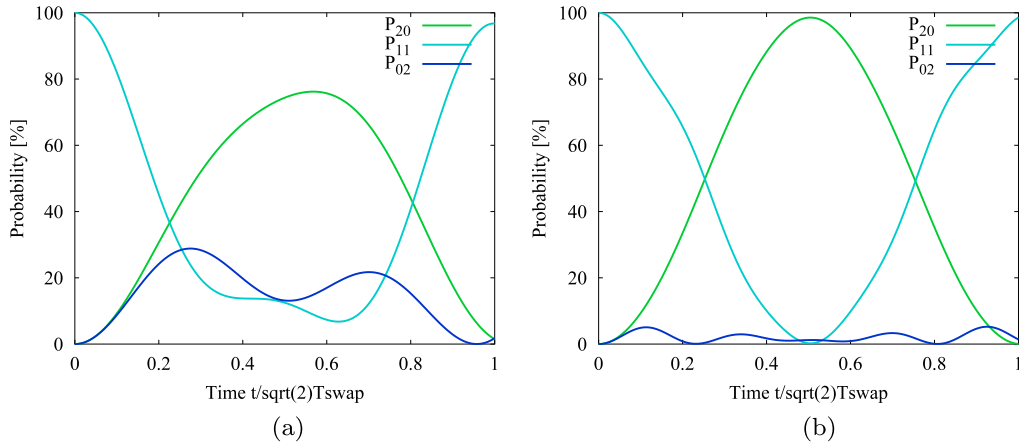


Figure 4. Time evolution of the populations computed using the spectrum of figure 3 at $\delta = -\Delta$. Time is normalized to the duration of a 2π rotation through the qubit's $|2\rangle$ state. If the anharmonicity is too small the effect of the second state of the bus will be large. This degrades the fidelity of the Strauch gate. (a) Population against time with -75 MHz anharmonicity and (b) population against time with -250 MHz anharmonicity.

second excited state of the qubit, i.e. $|1, 1\rangle \leftrightarrow |2, 0\rangle$. This is made possible by the anti-crossing indicated by the vertical black line in figure 3. This is when the qubit's $|1\rangle \leftrightarrow |2\rangle$ transition is on resonance with the bus. Here the additional level $|0, 2\rangle$ is an unwanted state; any population entering it will decrease the gate's fidelity. Hamiltonian (5) shows that the larger the anharmonicity is, the further away the $|0, 2\rangle$ state is detuned. To clearly see its influence, the time evolved population, shown in figure 4, is computed with $\delta = -\Delta$ and for two different values of Δ ; one small and one large. When Δ is small, the Strauch gate performs badly, as shown by figure 5. With -250 MHz anharmonicity the leakage to $|0, 2\rangle$ is at maximum 5%, which is still large. Figure 5 shows that the phase difference at the end of the 2π rotation between the time evolved state looping from and to $|1, 1\rangle$ and the reference $\exp[-i(2\omega_b - \Delta)t]$ has a small deviation from π . The discrepancy is due to leakage to the $|0, 2\rangle$ state. Such phenomena and multi-step swapping warrant a numerical approach to the problem of CZ gate design in the qubit–bus–qubit architecture, where

the full Hamiltonian up to $n = 2$ quanta is considered. Algorithms that maximize fidelity, such as GRAPE and the quasi-Newton BFGS method [37], naturally suppress leakage, which decreases fidelity [38] as defined.

3. Controlled-Z gate design by gradient ascent

Gradient ascent pulse shape engineering (GRAPE) numerically solves the problem of finding a control pulse that produces the desired time evolution operator within a given time [16]. In this work, the pulses are updated using the quasi-Newtonian BFGS method [39]. Hamiltonian (3) is separated into the drift and the two control parts \hat{n}_1 and \hat{n}_2 . This section describing the GRAPE implementation to the problem at hand covers the choice of fidelity function, the effect of the electronics and how to deal with nonlinearities arising when using phase qubits. We then apply gradient ascent to systems with different parameter values to illustrate key features of the system. We also benchmark the numerical pulses on a system corresponding to real qubits.

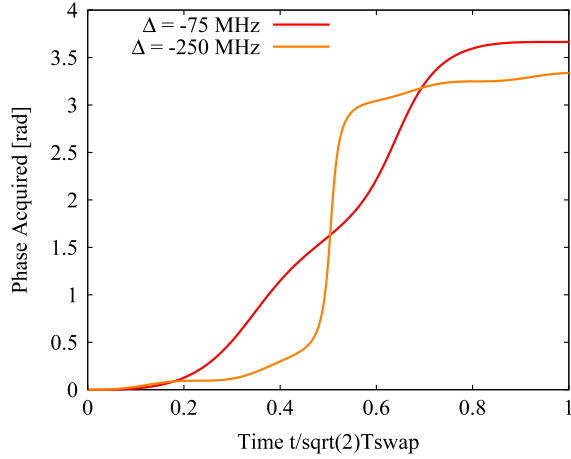


Figure 5. Phase difference between $|1, 1\rangle \exp\{-i\hat{H}t\}|1, 1\rangle$ and $\exp\{-i(2\omega_b - \Delta)t\}$. The discrepancy at the end of the gate is due to the presence of the unwanted $|2\rangle$ state of the bus.

3.1. Fidelity function

We consider only unitary evolution. Thus, the overlap between the ideal \hat{U}_{ideal} and achieved gate \hat{U} serves as a fidelity function [16]

$$\Phi = \frac{1}{d^2} \left| \text{Tr} \left\{ \hat{U}_{\text{ideal}}^\dagger \mathbb{P}_Q \hat{U} \mathbb{P}_Q \right\} \right|^2. \quad (6)$$

\mathbb{P}_Q projects the time evolution operator onto the computational sub-space of dimension d . Any leakage out of this sub-space will be detected as missing probability [38].

3.2. Including electronic transfer functions

The arbitrary waveform generator (AWG) creating the control pulses has a limited bandwidth. Additionally, the lines and remaining electronics between the AWG and qubits can distort the pulses. For this reason, the input control sent to the AWG will differ from the control applied by the qubits. To a good approximation, this transfer is described by a linear causal transfer function [40]. When optimizing the pulse shapes it must be ensured that the result is experimentally feasible. However, the nature of the problem would require including numerical derivatives of measured transfer function data in the pulse optimization. We avoid numerical derivatives by convolving the pulses with a Gaussian to suppress high frequencies

$$\delta_{\text{qubit}}(t) = \int_{-\infty}^{\infty} \exp\left\{-\frac{(t-\tau)^2}{2\sigma^2}\right\} \delta(\tau) d\tau. \quad (7)$$

δ_{qubit} is the pulse shape that the qubit should see. The gradient is found with the chain rule [41]. The standard deviation σ should be chosen to reflect the capabilities of the AWG. In an experimental implementation, it would be necessary to deconvolve the pulse in the qubit control software to take into account the true transfer function, which typically must be measured. If the bandwidth of the pulse given by the optimization algorithm is small, as guaranteed by our filtering procedure, then this deconvolution is easy and pulse shapes remain feasible.

3.3. Frequency dependent anharmonicity

When optimizing pulses for a system where part of the Hamiltonian depends nonlinearly on the controls, the gradient rules of [16] must take the nonlinearity into account. Such a situation can arise when optimizing pulses for phase qubits where the anharmonicity depends nonlinearly on the qubit frequency. Appendix A of [42] shows how to obtain the analytic formula of the gradient where the Hamiltonian depends linearly on the controls $\hat{H}(t) = \hat{H}_d + \sum_k \delta_k(t) \hat{H}_k$. Here it is shown how to include nonlinearities. We assume that in the Hamiltonian there are some parameters Δ_l that depend nonlinearly on the controls, i.e. $\Delta_l = \Delta_l(\{\delta_k(t)\})$. The total Hamiltonian at time $j\Delta T$ becomes

$$\hat{H}(j\Delta T) = \hat{H}_d + \sum_k \delta_{kj} \hat{H}_k + \sum_l \Delta_l(\{\delta_{kj}\}) \hat{H}_{l,\text{nl}}. \quad (8)$$

The gradient of the time evolution operator \hat{U}_j of time-slice j , with respect to pixel δ_{kj} of control k , is only sensitive to small variations around the value assumed by that pixel. Therefore we linearize the Hamiltonian at each iteration. If pixel kj assumes the value $\delta_{kj}^{(n)}$ at iteration n then the Hamiltonian can be approximated by $\hat{H}(j\Delta T) \simeq \hat{H}'_d + \sum_k \delta_{kj} \hat{H}'_k$, where the drift and controls of this linearized Hamiltonian are

$$\hat{H}'_d = \hat{H}_d + \sum_l \Delta_l(\{\delta_{kj}^{(n)}\}) \hat{H}_{l,\text{nl}}, \quad (9)$$

$$\hat{H}'_k = \hat{H}_k + \sum_l \left. \frac{\partial \Delta_l(\{\delta_{kj}\})}{\partial \delta_{kj}} \right|_{\delta_{kj}^{(n)}} \hat{H}_{l,\text{nl}}. \quad (10)$$

This enables us to compute the gradient using the rules given in [16, 42]. At each iteration the control fields change and so do the linearized Hamiltonians \hat{H}'_d and \hat{H}'_k .

In the case of phase qubits, the dependency of the anharmonicity Δ_k on the qubit frequency δ_k can either be found numerically with a discrete variable representation [43] of the qubit's full potential or through measurement with high-power spectroscopy [44].

3.4. Numerical results

Here we assume that both qubits have the same anharmonicity $\Delta_1 = \Delta_2 = \Delta = -0.1\omega_b$ and coupling $g_1 = g_2 = g = 0.02\omega_b$. Time will be indicated in dimensionless units of tg , with g in radians s^{-1} . The desired gate fidelity is $1-10^{-4}$. At the start and end of the gate both qubits are far off resonance at their parking frequencies. This is included in the code by adding several buffer pixels, held at a constant detuning, before and after the gate.

The control pulses, found without Gaussian convolution, for a gate time of $9\ tg$ are shown in figure 6(a). Figure 6(b) shows the discrete Fourier transform (DFT) of these pulses: most of the oscillations in $\delta_1(t)$ and $\delta_2(t)$ have frequency components of the order of the qubit–bus coupling constant $g/\sqrt{2}$. This is because the CZ gate is made using $|2\rangle$ states.

Figure 6 shows that the controls for qubit 2 oscillate at a much larger amplitude than those for qubit 1. We will later

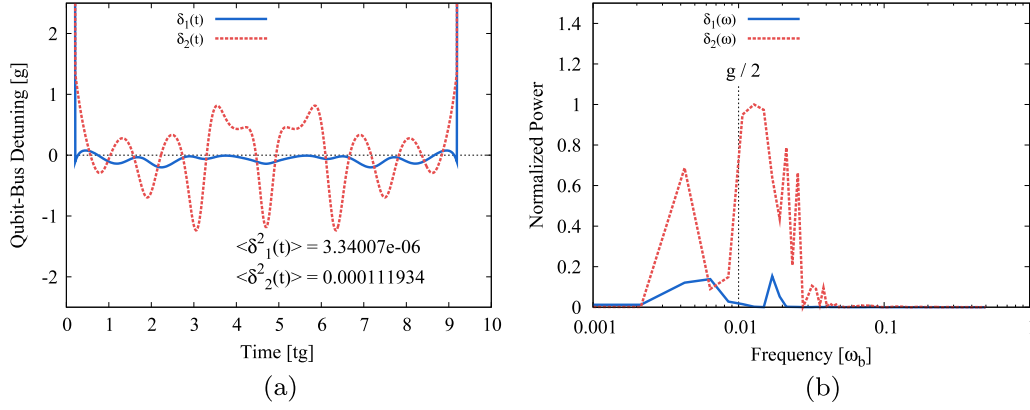


Figure 6. (a) Control pulses for a gate time slightly above T_{QSL} . (b) Discrete Fourier transform of (a) showing that most of the spectral power is at small frequencies of the order of g .

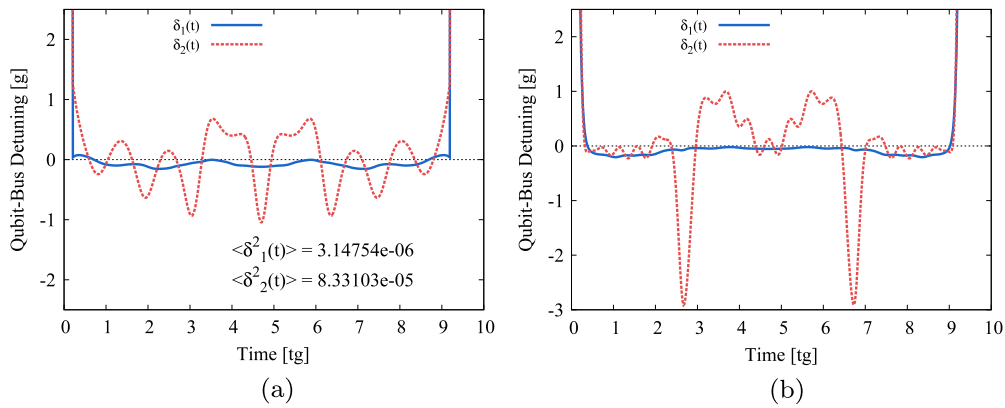


Figure 7. Comparison of the choice of Ginger and Fred. (a) $(\Delta_1, \Delta_2) = (-0.3, -0.1)$. Qubit 2, chosen as Fred, is the most linear. The optimization was successful, reaching $\Phi = 99.99\%$. (b) $(\Delta_1, \Delta_2) = (-0.1, -0.3)$. Qubit 2, chosen as Ginger, is the most linear. The optimization was unsuccessful, reaching only 99.95%. In both cases asymmetric initial conditions were used to force GRAPE to choose qubit 2 as Fred. Only the case shown in figure (a) resulted in good convergence.

demonstrate that qubit 2 and the resonator populate their $|2\rangle$ states similarly to the Strauch gate in the pulse sequence. As the CZ gate is symmetric under the exchange of qubits, a control-target terminology to distinguish these qubits would be inappropriate. Instead, the qubit with smaller oscillations will be referred to as *Ginger* whereas the other will be called *Fred*. Section 3.4.1 explores what motivates the symmetry breaking apparent in these pulses.

3.4.1. Effect of anharmonicity. As just stated, the CZ gate is symmetric under qubit exchange, however, the underlying Hamiltonian need not be. The main aspect breaking the symmetry is the anharmonicity of the qubit. This was studied with several different combinations of qubit anharmonicities: $\Delta_1, \Delta_2 \in \{-0.1, -0.2, -0.3\}$. The allowed gate time was 9 tg . Because the Strauch method uses the $|2\rangle$ state of the bus, the more linear qubit takes on the role of Fred since it is easier to drive the $|1, 1\rangle \leftrightarrow |0, 2\rangle$ transition with the bus. The reason is: the greater the anharmonicity, the more the qubit has to move away from the $\delta = 0$ qubit–bus resonance, which is also crucial for $|0, 1\rangle \leftrightarrow |1, 0\rangle$ exchanges. Figures 7(a) and (b) show two pulses for which $(\Delta_1, \Delta_2) = (-0.3, -0.1)$ and $(\Delta_1, \Delta_2) = (-0.1, -0.3)$ respectively. In both cases the

search was nudged by means of asymmetric initial conditions, to choose qubit 2 as Fred. In the first case, when the most linear qubit was chosen as Fred the target gate error of 10^{-4} was reached. When the wrong qubit was assigned as Fred in the initial conditions, the code was not able to reach the target gate fidelity, reaching only $1 - \Phi \simeq 5.5 \times 10^{-3}$. The choice as to which qubit assumes which role can either be enforced through asymmetric initial conditions or left up to GRAPE/BFGS with symmetric initial conditions. In the latter case the algorithm converges more slowly in the initial steps before numerical approximations break the symmetry. The anharmonicity of Ginger does not play such an important role as that of Fred. Figure 6 shows a pulse with $(\Delta_1, \Delta_2) = (-0.1, -0.1)$. The pulse of Fred is almost identical to the one in figure 7(a). However, since Ginger is more linear than in figure 7(a) its control pulse has picked up some additional modulation which could be interpreted as minimizing leakage to the qubit $|2\rangle$ state.

The populations associated with the pulse shown in figure 7(a) are displayed in figure 8; the $|2\rangle$ state of the bus is highly used. Some of the excitation is transferred to the $|2\rangle$ state of Fred, but the $|2\rangle$ state of Ginger remains empty, confirming our interpretation of the role of both qubits.

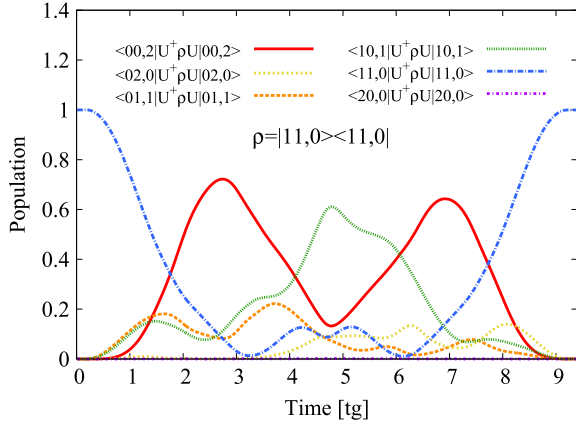


Figure 8. Populations assuming the input state is $\rho_{\text{in}} = |11, 0\rangle\langle 11, 0|$ for the pulse of figure 7(a). It shows that the $|2\rangle$ state of the bus is highly solicited to realize the CZ gate. However, the $|2\rangle$ state of the most nonlinear qubit is not used at all.

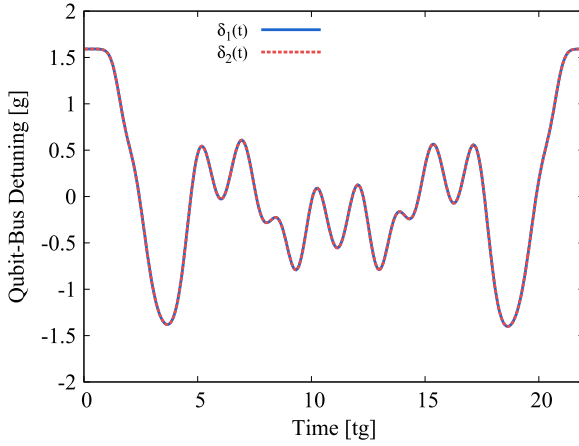


Figure 9. Control pulse with perfect fidelity (up to machine precision) for identical qubits and symmetric initial conditions. The control pulses producing the CZ gate are identical for both qubits, showing that the two pulses need not be asymmetric. The qubit parameters were $g_1/2\pi = g_2/2\pi = 50$ MHz and $\Delta_1 = \Delta_2 = 60$ MHz.

However, the pulses need not be asymmetric. If both qubits are identical and the initial conditions are symmetric, the resulting pulse sequence will be symmetric. Such a symmetric pulse is shown in figure 9.

3.4.2. Influence of impulse response.. As can be seen from figure 6(b) the DFT of the unfiltered pulse has almost all its power at low frequencies. This suggests that introducing a filter function in GRAPE should not significantly degrade the gate's performance. Therefore, in the control landscape, the optimal solutions with and without the filter function should lie close together. The procedure is first to search for a pulse without the filter function and then to rerun the optimization with the filter function using the previously found pulse as the initial condition. The Gaussian impulse response has a standard deviation of $\sigma \cong 4\omega_b^{-1}$, chosen so that the 3 dB attenuation lies slightly above $g = 0.02\omega_b$. This function was then used to find a pulse sequence with

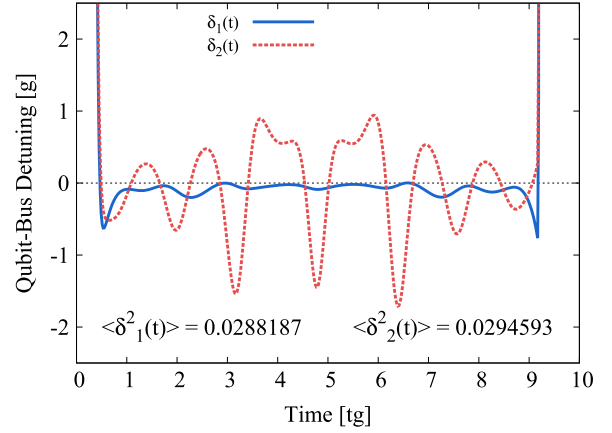


Figure 10. Effect of the filter function on the pulse sequence. The pulse from figure 6 was used as a starting point for the gradient ascent. Given that most of the spectral weight was initially at low frequencies, the Gaussian convolution has hardly any effect and the target fidelity of 99.99% is retrieved after only a few iterations.

Table 1. Parameters of the phase qubits. These values were used in the pulses presented in this document. The swap bus time T_{swap} is the time required to swap a quanta between the qubit and bus, i.e. $|1, 0\rangle \rightarrow |0, 1\rangle$. It is related to the coupling strength by $g_k = (2T_{\text{swap},k})^{-1}$.

Element	Parameter	Value	Unit
Bus	ω_b Frequency	6.1	GHz
Qubit 1	ω_1 Parking frequency	6.778	GHz
	Δ_1 Anharmonicity	-71	MHz
	Swap bus time	12.6	ns
	g_1 Coupling strength	40	MHz
Qubit 2	ω_2 Parking frequency	6.607	GHz
	Δ_2 Anharmonicity	-59	MHz
	Swap bus time	9.2	ns
	g_2 Coupling strength	54	MHz

the pulses shown in figure 6 as starting point. The output is shown in figure 10. As seen from the figures, the pulse found with the filter function is almost identical to the one found with a perfect impulse response. However, the sharp corners have been smoothed out due to the high-frequency filtering. This is encouraging since typical AWGs have a bandwidth of 500 MHz and most coupling strengths are in the range 20–70 MHz. Given the small effect of the impulse response, the subsequent optimization will be done in one step using Gaussian convolution.

3.5. Benchmarking

To benchmark the performance of the numerical pulses against existing pulses, the GRAPE method is applied to phase qubits in the RezQu architecture. The values³ for the parameters in the Hamiltonian are shown in table 1. The nonlinear behaviour of the qubit's anharmonicity was determined by high-power spectroscopy [44]. The anharmonicities for this chip are very low and as indicated

³ The values for the parameters in the Hamiltonian correspond to a sample of the John Martinis group.

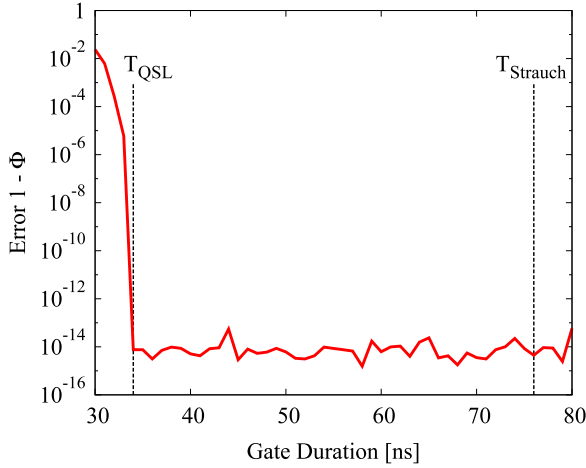


Figure 11. Scan of the gate duration to find the quantum speed limit for phase qubits with the values of table 1. The found quantum speed limit $T_{\text{QSL}} = 34$ ns is twice as fast as the sequential pulse using the Strauch gate, which takes $T_{\text{Strauch}} = 76$ ns. Above the quantum speed limit, the numerical pulses are perfect up to machine precision.

from section 2.3, would produce Strauch gates with extremely low fidelities.

In some situations the time it takes for a given state to evolve into an orthogonal state is bounded from below. This lower bound is the quantum speed limit (QSL) [45, 46]. This sets a minimum time T_{QSL} in which a gate can be done. When the gate time is above this speed limit, numerical pulses have perfect fidelity up to machine precision. This is shown in figure 11, where the gate time is progressively decreased. As long as $T_{\text{Gate}} > T_{\text{QSL}}$ the pulse error is zero down to machine precision. For the system with values given by 1, the QSL is less than half of the time it takes the analytic pulse sequence of figure 2. We find $T_{\text{QSL}} = 34$ ns. Below the quantum speed limit the fidelity degrades very rapidly. An error-free (up to machine precision) pulse is shown in figure 12(a). As seen in figure 12(b), a DFT shows that

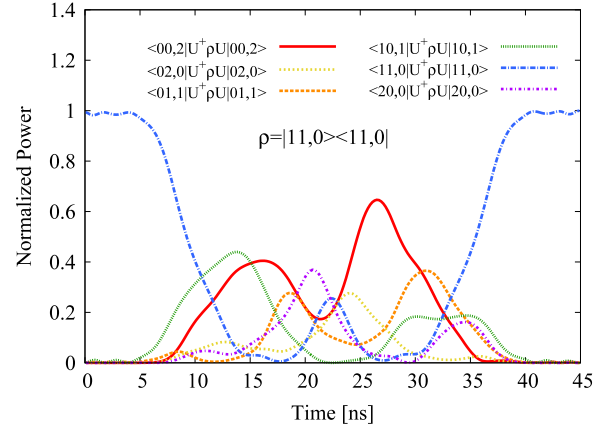


Figure 13. Populations of the two-excitation sub-space associated with the GRAPE pulse shown in figure 12(a). As can be seen, an analytical picture similar to that shown in section 2.2 is no longer possible.

there is hardly any spectral power above 500 MHz, thus making the pulse experimentally realistic. Figure 13 shows the populations in the two-excitation sub-space, illustrating the increased complexity of these fast gates, defying, for now, a simple physical picture.

Note that in some cases, in particular for transmons that are operated through the resonator requiring a somewhat open resonator, one may desire an idle frequency that is more detuned from the resonator than assumed here. This would lead to slightly steeper initial and final slopes, but does not change our conclusions.

4. Error sources and mitigation strategies

Section 3.5 showed that CZ gates with arbitrary intrinsic fidelities can be generated even for low anharmonicity qubits. However, in experimental conditions these high-quality pulses

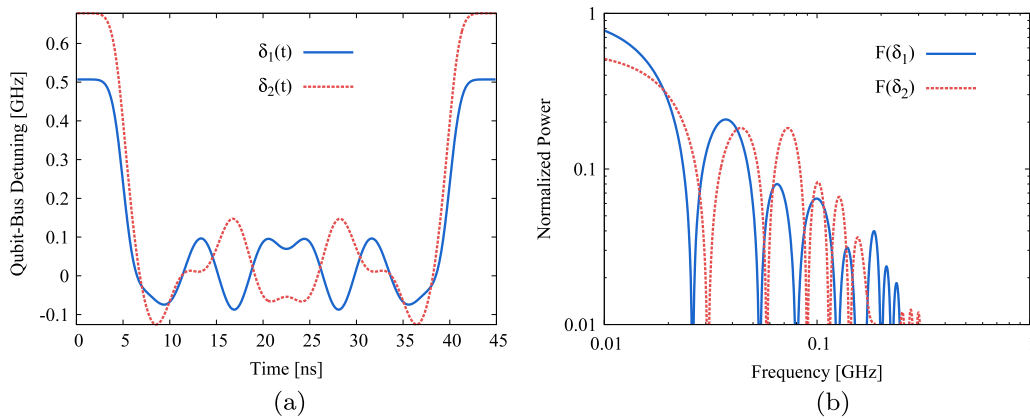


Figure 12. Summary of a numerical CZ gate design. Despite the low anharmonicities the pulses are able to reach very high fidelities. (a) Control pulse with $1-10^{-14}$ intrinsic fidelity. The gate time is slightly above the quantum speed limit, i.e. $T_{\text{Gate}} = 35$ ns. (b) Normalized spectrum of the ZPA corresponding to the GRAPE pulse shown in (a). Almost all the spectral power is within a few hundred MHz, thus the pulse is experimentally feasible.

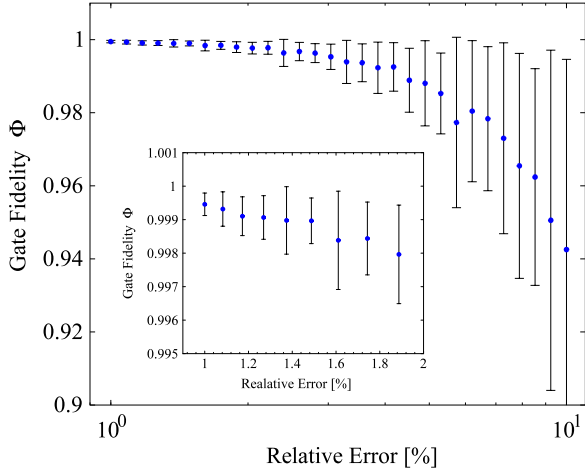


Figure 14. Error introduced by randomly changing the amplitude of the controls. The relative error is expressed in $\Delta\delta_{k_j}/\delta_{k_j}$. The system considered was the qubit–bus–qubit with constant anharmonicity.

are rapidly degraded by various errors. Section 4.1 reviews them and discusses how to overcome them.

4.1. Intrinsic pulse robustness

Gradient ascent engineered pulses enjoy an almost null first derivative with respect to the individual control pixels. Thus, to first order, random fluctuations of the pulse amplitude do not severely impact the fidelity. This was checked by perturbing the controls with white Gaussian noise with a standard deviation given by $\sigma_E = \Delta\delta_{k_j}/\delta_{k_j}$. Figure 14 shows that a 1% relative variation of the control field amplitude decreases a 99.99% intrinsic fidelity pulse to 99.95%. Therefore, random fluctuations in pulse amplitude are of little consequence on these pulses [47, 48].

4.2. Systematic errors

Some systematic errors will effect the pulses in a more significant way than the random fluctuations of pulse amplitude. There are three main errors that have been identified: calibration errors, timing errors and parameter errors. All are described below.

4.2.1. Calibration errors: control pulse amplitude to qubit frequency. Although we optimize the qubit frequency in our numerics, the true control is the amplitude of the Z pulse (ZPA), a voltage pulse applied to the qubit. The ZPA is related to the frequency of the qubit through a calibration curve. This curve must be measured using spectroscopy and errors in it will cause errors in the qubit frequency (see figure 15 for a sketch). The bus frequency does not enter the Hamiltonian (3). However, it must be known so as to give the qubits the right ZPA to put them on resonance with the bus. A constant and systematic shift of the pulse with respect to the resonance point produces phase and leakage errors. The situation is sketched in figure 16, where qubit 1 undershoots the bus by an amount $\Delta\omega_{b,1}$ and qubit 2 overshoots the bus by $\Delta\omega_{b,2}$.

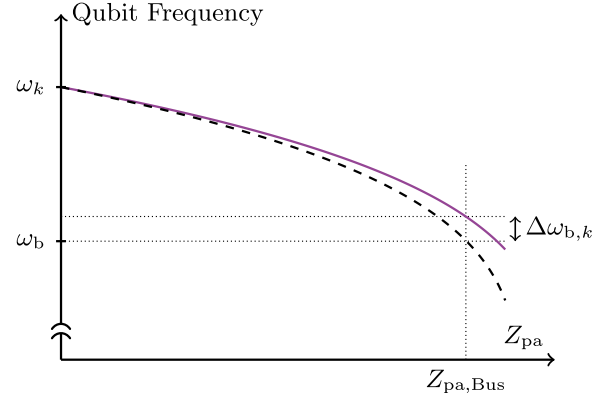


Figure 15. Calibration errors result in a DC offset of the pulse. The ‘true’ calibration curve—dashed line—is approximated by the solid line, which is the measured calibration curve. This discrepancy causes the qubit–bus resonance to be missed by $\Delta\omega_{b,k}$.

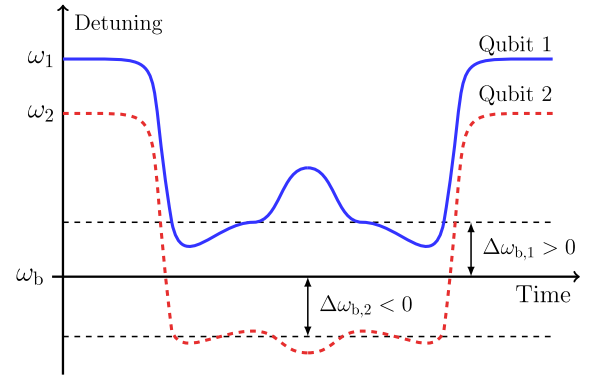


Figure 16. DC offset in the pulse amplitudes. The qubit parking frequency ω_{Q_k} is left unchanged. However, the resonance point is missed; the pulses perform their oscillations around $\omega_b + \Delta\omega_{b,k}$ instead of ω_b .

Off resonance from the bus, calibration errors have little effect since qubit and resonator cannot exchange quanta. Therefore this error is modelled by a systematic shift in the qubit frequency, changing the resonance point with the bus

$$\delta_k(t) \mapsto \delta_k(t) + \Delta\omega_{b,k}. \quad (11)$$

This shift also displaces the qubit parking frequency, which, in experiment, is typically held constant at all times [49]. This discrepancy between experiment and model is acceptable due to the lack of exchange of quanta far off resonance. The Hamiltonian with error terms is

$$\begin{aligned} \hat{H}^R = & \underbrace{\sum_{k=1}^2 \delta_k(t) \hat{n}_k}_{\text{Controls}} \\ & + \underbrace{\sum_{k=1}^2 \left[\Delta\omega_{b,k} \hat{n}_k + \Delta_k \hat{\Pi}_{2,k} + \frac{g_k}{2} (\hat{\sigma}_k^+ \hat{a}_b + \hat{\sigma}_k^- \hat{a}_b^\dagger) \right]}_{\text{Drift with errors}}. \end{aligned} \quad (12)$$

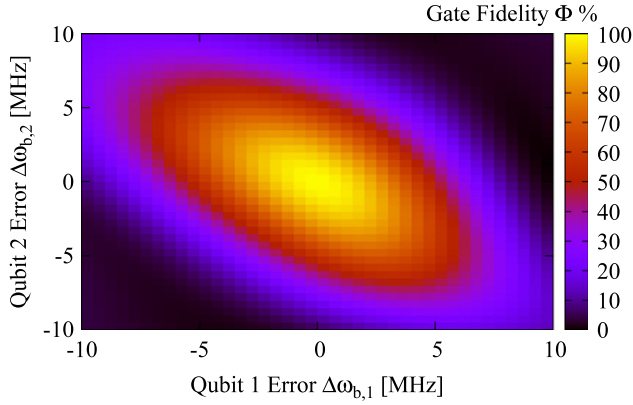


Figure 17. Loss of fidelity due to overshoot and undershoot of the bus–qubit resonance frequency arising from systematic calibration errors. As can be seen, errors on the bus frequency of less than 0.1% ruin the pulses.

The effect of the calibration error on the fidelity (6) is shown in figure 17. A pulse was first optimized with $(\Delta\omega_{b,1}, \Delta\omega_{b,2}) = (0, 0)$ and then the fidelity is recomputed for different values of the error. The central high-fidelity region is very small; although the first derivative $\partial\Phi/\partial\Delta\omega_{b,k}$ is close to zero near the optimum the second derivative is very strong. This shows how small errors ruin the pulse.

If a single control amplitude at a given time is viewed as a degree of freedom, pulse optimization is a highly under-constrained nonlinear problem, given the limited number of independent parameters in the target gate. Robust control exploits the surplus of degrees of freedom to make a pulse sequence robust over a larger parameter range [50]. However, in this case such methods fail since the error is on the control Hamiltonians and not the drift. To remove the calibration error a different approach must be used.

We propose to manually introduce a controllable DC offset in the pulse. The effect of this offset on various quantities can be determined both in simulations and experiment. Comparing the two gives the optimal DC offset needed to compensate the error. In simulation, we compute the time evolution operator, which lets us know how big

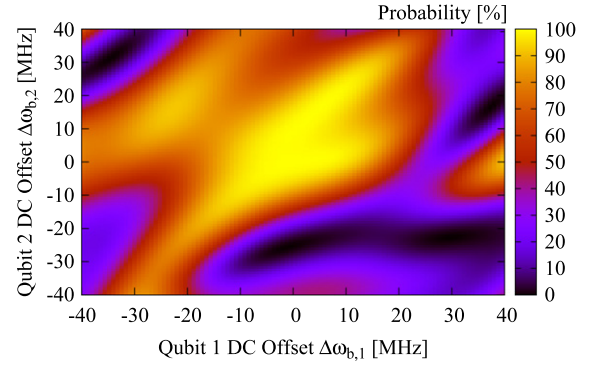


Figure 18. Scan of $|U_{10,10}|^2$ as a function of the calibration error. Away from the resonance point $(\Delta\omega_{b,1}, \Delta\omega_{b,2}) = (0, 0)$ leakage starts to manifest itself as a decrease in $|U_{10,10}|^2$. The many features in the plot allow a good correction of the error.

leakage and phase errors are. In an experiment, leakage can be measured by qubit population and phases are accessible with Ramsey measurements.

We illustrate this first with the qubit population by scanning $(\Delta\omega_{b,1}, \Delta\omega_{b,2})$ and computing the population of qubit 1 after the gate. Figure 18 shows the magnitude of $[\hat{U}]_{10,10}$. It is the entry of the time evolution operator quantifying population transfer from state $|10, 0\rangle$ to itself. For an ideal CZ $|[\hat{U}]_{10,10}|^2 = 1$ —however, when changing the DC offset this value decreases. The strong effect of the error is thus used to our advantage, since the many features in the $(\Delta\omega_{b,1}, \Delta\omega_{b,2})$ error landscape allow an easy comparison between experiment and simulation. Similar data could be obtained with an experiment, comparing it to the simulation would give the DC offset needed to correct the errors.

4.2.2. Timing errors.. Another error source is the relative timing between the two pulses. This arises if the wires taking pulse 1 from the AWG to qubit 1 differ in length from those to qubit 2. Pulses offset in time by $\Delta\tau$, as sketched in figure 19(a), lose their fidelity, as shown by figure 19(b). This error can be removed by introducing a time shift between the

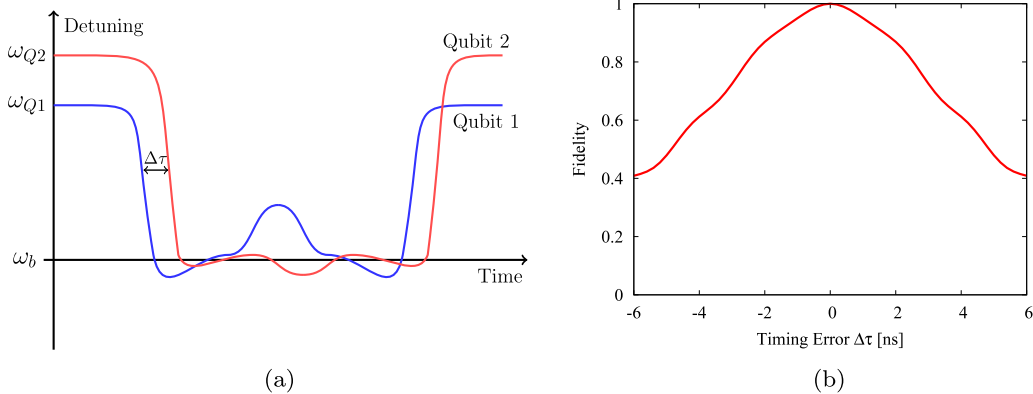


Figure 19. Relative timing errors. (a) Sketch of pulse relative timing errors. Both pulses have the intended shape but are offset in time by an amount $\Delta\tau$. (b) Degradation of the fidelity as a function of the timing error.

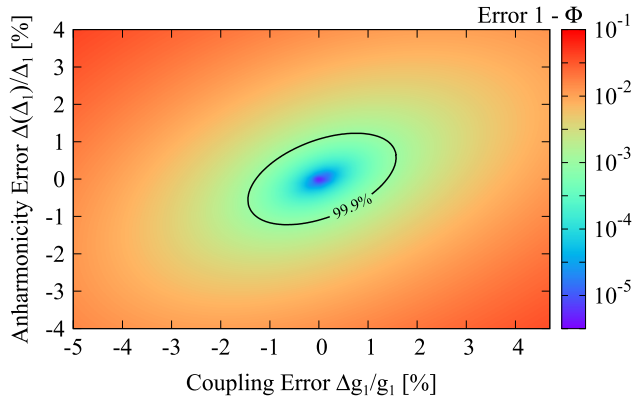


Figure 20. Degradation in fidelity due to errors in the parameters of the Hamiltonian. The pulse was optimized with a target error of 10^{-5} . If a fidelity of 99.9% is sufficient, the intrinsic robustness of the pulse can support errors of up to 1.5% in coupling strength and 1.2% in anharmonicity.

pulses and scanning the time shift until leakage/fidelity is minimized/optimized. As seen from figure 19(b) the relative timing between the pulses should be accurate to within ≈ 100 ps.

4.2.3. Hamiltonian parameter errors.. Gradient ascent engineered pulses rely on knowing the Hamiltonian to optimize the pulse. However, the parameters entering the model need to be measured and thus come with some amount of uncertainty and error. The pulses designed with these parameters will perform sub-optimally. In the qubit–bus–qubit system, there are four parameters that are susceptible to these error: $\{\Delta_1, \Delta_2, g_1, g_2\}$. For instance, figure 20 shows fidelity degradation as a function of errors on the coupling strength and anharmonicity of qubit 1. The pulse was optimized to have a target error of 10^{-5} . If a pulse fidelity of 99.9% is sufficient, the intrinsic pulse robustness, i.e. $\partial\Phi/\partial g_k \approx 0$ and $\partial\Phi/\partial\Delta_k \approx 0$, allows us to tolerate an error of up to 1.5% in coupling strength and 1.2% in anharmonicity.

5. Conclusions

We develop fast pulses implementing an entangling gate, the CZ, between two qutrits through a bus. These demonstrate a factor of two speed up in CZ gates as well as the possibility to reach arbitrary intrinsic gate fidelity as long as the gate time is above the quantum speed limit. It turns out that the optimal pulses break the symmetry of the target gate and make active use of non-computational excited states. We have also shown how errors arising from realistic experimental conditions can be negated.

The controls we found typically lead to occupation of the resonator during gate operation. This may be a disadvantage if there is strong Purcell decay from the cavity, as necessitated in architectures where control and/or readout are done through the cavity [3, 1, 15]. However, it is not a limitation in situations when control and readout are done directly on the qubits and the main decoherence sources are connected to the qubits themselves [49, 33]. In the former case, one would like to keep

the qubits far detuned from the cavity and use a dispersive gate [21]. The precise crossover between these regimes and optimality under decay are topics for future research. Further work in cavity-mediated gates [21, 28] discusses a variety of strategies found by hand, smooth few-parameter pulses that all take longer times and are less adapted to imperfections of the system and thus may be a stepping stone towards optimized gates.

This research was funded by the Office of the Director of National Intelligence (ODNI), Intelligence Advanced Research Projects Activity (IARPA), through the Army Research Office. All statements of fact, opinion or conclusions contained herein are those of the authors and should not be construed as representing the official views or policies of IARPA, the ODNI, or the US Government.

Acknowledgments

We acknowledge continued collaboration with D Sank and J M Martinis, as well as useful discussions with E J Pritchett, S T Merkel and M R Geller. We thank Christine Ridder for the implementation of BFGS. This work was supported by IARPA through the MQCO and the EU through the SCALEQIT program.

References

- [1] Schoelkopf R J and Girvin S M 2008 Wiring up quantum systems *Nature* **451** 664–9
- [2] Clarke J and Wilhelm F K 2008 Superconducting quantum bits *Nature* **453** 1031–42
- [3] Blais A, Huang R-S, Wallraff A, Girvin S M and Schoelkopf R J 2004 Cavity quantum electrodynamics for superconducting electrical circuits: an architecture for quantum computation *Phys. Rev. A* **69** 062320
- [4] Nakamura Y, Pashkin Y A and Tsai J S 1999 Coherent control of macroscopic quantum states in a single-Cooper-pair box *Nature* **398** 786
- [5] Vion D, Aassime A, Cottet A, Joyez P, Pothier H, Urbina C, Esteve D and Devoret M H 2002 Manipulating the quantum state of an electrical circuit *Science* **296** 866
- [6] Bertet P, Chiorescu I, Burkard G, Semba K, Harmans C J P M, DiVincenzo D P and Mooij J E 2005 Relaxation and dephasing in a flux-qubit *Phys. Rev. Lett.* **95** 257002
- [7] Houck A A, Koch J, Devoret M H, Girvin S M and Schoelkopf R J 2009 Life after charge noise: recent results with transmon qubits *Quantum Inf. Process.* **8** 105
- [8] Bylander J, Gustavsson S, Yan F, Yoshihara F, Harrabi K, Fitch G, Cory D G, Nakamura Y, Tsai J-S and Oliver W D 2011 Noise spectroscopy through dynamical decoupling with a superconducting flux qubit *Nature Phys.* **7** 565–70
- [9] Paik H *et al* 2011 Observation of high coherence in Josephson junction qubits measured in a three-dimensional circuit QED architecture *Phys. Rev. Lett.* **107** 240501
- [10] Masluk N A, Pop I M, Kamal A, Mineev Z K and Devoret M H 2012 Microwave characterization of Josephson junction arrays: implementing a low loss superinductance *Phys. Rev. Lett.* **109** 137002
- [11] Stock R and James D F V 2009 Scalable, high-speed measurement-based quantum computer using trapped ions *Phys. Rev. Lett.* **102** 170501
- [12] Clarke J and Wilhelm F K 2008 Superconducting qubits *Nature* **453** 1031

- [13] Makhlin Yu, Schön G and Shnirman A 2001 Quantum-state engineering with Josephson-junction devices *Rev. Mod. Phys.* **73** 357
- [14] Devoret M H and Martinis J M 2004 Implementing qubits with superconducting integrated circuits *Quantum Inf. Process.* **3** 163–203
- [15] Devoret M H and Schoelkopf R J 2013 Superconducting circuits for quantum information: an outlook *Science* **339** 1169
- [16] Khaneja N, Reiss T, Kehlet C, Schulte-Herbrüggen T and Glaser S J 2005 Optimal control of coupled spin dynamics: design of NMR pulse sequences by gradient ascent algorithms *J. Magn. Reson.* **172** 296–305
- [17] Rice S A and Zhao M 2000 *Optical Control of Molecular Dynamics* (New York: Wiley)
- [18] Brumer P and Shapiro M 2003 *Principles of the Quantum Control of Molecular Processes* (New York: Wiley)
- [19] Sillanpää M A, Park J I and Simmonds R W 2007 Coherent quantum state storage and transfer between two phase qubits via a resonant cavity *Nature* **449** 438
- [20] Majer J *et al* 2007 Coupling superconducting qubits via a cavity bus *Nature* **449** 443
- [21] Blais A, Gambetta J, Wallraff A, Schuster D I, Girvin S M, Devoret M H and Schoelkopf R J 2007 Quantum-information processing with circuit quantum electrodynamics *Phys. Rev. A* **75** 032329
- [22] Plantenberg J H, de Groot P C, Harmans C J P M and Mooij J E 2007 Demonstration of controlled-not quantum gates on a pair of superconducting quantum bits *Nature* **447** 836–9
- [23] Liu Y-X, Wei L F, Tsai J S and Nori F 2006 Controllable coupling between flux qubits *Phys. Rev. Lett.* **96** 067003
- [24] Chow J M *et al* 2011 Simple all-microwave entangling gate for fixed-frequency superconducting qubits *Phys. Rev. Lett.* **107** 080502
- [25] Dewes A, Lauro R, Ong F R, Schmitt V, Milman P, Bertet P, Vion D and Esteve D 2012 Quantum speeding-up of computation demonstrated in a superconducting two-qubit processor *Phys. Rev. B* **85** 140503(R)
- [26] DiCarlo L *et al* 2009 Demonstration of two-qubit algorithms with a superconducting quantum processor *Nature* **460** 240
- [27] Fedorov A, Steffen L, Baur M, da Silva M P and Wallraff A 2012 Implementation of a Toffoli gate with superconducting circuits *Nature* **481** 170
- [28] Ghosh J, Galiatdinov A, Zhou Z, Korotkov A N, Martinis J M and Geller M R 2013 High-fidelity controlled- σ Z gate for resonator-based superconducting quantum computers *Phys. Rev. A* **87** 022309
- [29] Vidal G and Dawson C M 2004 Universal quantum circuit for two-qubit transformations with three controlled-not gates *Phys. Rev. A* **69** 010301
- [30] Raimond J M, Brune M and Haroche S 2001 Manipulating quantum entanglement with atoms and photons in a cavity *Rev. Mod. Phys.* **73** 565
- [31] Frey T, Leek P J, Beck M, Blais A, Ihn T, Ensslin K and Wallraff A 2012 Dipole coupling of a double quantum dot to a microwave resonator *Phys. Rev. Lett.* **108** 046807
- [32] Petersson K D, McFaul L W, Schroer M D, Jung M, Taylor J M, Houck A A and Petta J R 2012 Circuit quantum electrodynamics with a spin qubit *Nature* **490** 380
- [33] Mariantoni M *et al* 2011 Implementing the quantum von Neumann architecture with superconducting circuits *Science* **334** 61–5
- [34] Koch J, Yu T M, Gambetta J, Houck A A, Schuster D I, Majer J, Blais A, Devoret M H, Girvin S M and Schoelkopf R J 2007 Charge-insensitive qubit design derived from the Cooper pair box *Phys. Rev. A* **76** 042319
- [35] Martinis J M, Nam S, Aumentado J and Urbina C 2002 Rabi oscillations in a large Josephson-junction qubit *Phys. Rev. Lett.* **89** 117901
- [36] Strauch F W 2003 Quantum logic gates for coupled superconducting phase qubits *Phys. Rev. Lett.* **91** 167005
- [37] Nocedal J and Stephen S W 2006 *Numerical Optimization* 2nd edn (New York: Springer)
- [38] Rebertrost P and Wilhelm F K 2009 Optimal control of a leaking qubit *Phys. Rev. B* **79** 060507
- [39] Nocedal J 1980 Updating quasi-Newton matrices with limited storage *Math. Comput.* **35** 773
- [40] Gustavsson S, Zwier O, Bylander J, Yan F, Yoshihara F, Nakamura Y, Orlando T P and Oliver W D 2013 Improving quantum gate fidelities by using a qubit to measure microwave pulse distortions *Phys. Rev. Lett.* **110** 040502
- [41] Motzoi F, Gambetta J M, Merkel S T and Wilhelm F K 2011 Optimal control methods for rapidly time-varying Hamiltonians *Phys. Rev. A* **84** 022307
- [42] Machnes S, Sander U, Glaser S J, de Fouquières P, Gruslys A, Schirmer S and Schulte-Herbrüggen T 2011 Comparing, optimising and Benchmarking quantum control algorithms in a unifying programming framework *Phys. Rev. A* **84** 022305
- [43] Colbert D T and Miller W H 1991 A novel discrete variable representation for quantum mechanical reactive scattering via the S-matrix Kohn method *J. Chem. Phys.* **96** 1982–91
- [44] Yamamoto T *et al* 2010 Quantum process tomography of two-qubit controlled-Z and controlled-not gates using superconducting phase qubits *Phys. Rev. B* **82** 184515
- [45] Schulman L S 2008 Jump time and passage time: the duration of a quantum transition *Lect. Notes Phys.* **734** 107–28
- [46] Vaidman L 1992 Minimum time for the evolution to an orthogonal quantum state *Am. J. Phys.* **60** 182
- [47] Spörl A, Schulte-Herbrüggen T, Glaser S J, Bergholm V, Storz M J, Ferber J and Wilhelm F K 2007 Optimal control of coupled Josephson qubits *Phys. Rev. A* **75** 012302
- [48] Montangero S, Clarco T and Fazio R 2007 Robust optimal quantum gates for Josephson charge qubits *Phys. Rev. Lett.* **99** 170501
- [49] Galiatdninov A, Korotkov A N and Martinis J M 2012 Resonator/zero-qubit architecture for superconducting qubits *Phys. Rev. A* **85** 042321
- [50] Khani B, Merkel S T, Motzoi F, Gambetta Jay M and Wilhelm F K 2012 High-fidelity quantum gates in the presence of dispersion *Phys. Rev. A* **85** 022306